

## Highlights from Gamma-ray Observation by the Tibet AS $\gamma$ Experiment

---

**M. Takita<sup>15,\*</sup> on behalf of the Tibet AS $\gamma$  Collaboration**

(a complete list of authors can be found at the end of the proceedings)

*E-mail:* [takita@icrr.u-tokyo.ac.jp](mailto:takita@icrr.u-tokyo.ac.jp)

The Tibet AS $\gamma$  experiment is located at 4,300 m above sea level, in Tibet, China. The experiment is composed of a 65,700 m<sup>2</sup> surface air shower array and 3,400 m<sup>2</sup> underground water Cherenkov muon detectors. The surface air shower array is used for reconstructing the primary particle energy and direction, while the underground muon detectors are used for discriminating gamma-ray induced muon-poor air showers from cosmic-ray (proton, helium,...) induced muon-rich air showers. Recently, the Tibet AS $\gamma$  experiment successfully observed gamma rays in the 100 TeV region from some point/extended sources as well as sub-PeV diffuse gamma rays along the Galactic disk. In this proceedings paper, the observational results will be presented, followed by some future prospect.

*37<sup>th</sup> International Cosmic Ray Conference (ICRC 2021)*  
*July 12th – 23rd, 2021*  
*Online – Berlin, Germany*

---

\*Presenter

## 1. Introduction

Cosmic rays were discovered in 1912 [1]. The energy spectrum at Earth is approximately expressed by a power-law function from  $10^9$  eV up to  $10^{20}$  eV. The spectral break points around 4 PeV, 100 PeV and a few EeV are named “Knee”, “second Knee” and “ankle”. The Knee was discovered in 1958 [2] and cosmic rays below the Knee are believed to be of galactic origin. Therefore, there should exist energetic celestial objects which accelerate cosmic rays up to PeV energies, called Pevatrons. Recently, Fermi-LAT found evidence that cosmic rays below 1 to 10 TeV region come from SNRs [3]. However, PeVatrons have not been detected in spite of extensive searches over 20 years in the 21<sup>st</sup> century.

Cosmic rays are supposed to be accelerated up to the Knee energy (PeV) region at cosmic-ray acceleration sites (for example, supernova remnants (SNRs), star-formation regions, the galactic center in our galaxy). Therefore, we naturally expect gamma rays above 100 TeV which originate in  $\pi^0$  decays produced by the accelerated cosmic rays interacting with interstellar matter surrounding the acceleration sites. The gamma-ray emission of electron origin may be highly suppressed above 10 TeV due to rapid decrease of inverse-Compton cross section by the Klein-Nishina effect as well as synchrotron radiation energy loss in the strong magnetic field around the acceleration sites. The detection and spectral measurement of gamma rays in the sub-PeV/PeV region from their celestial sources, together with multi-wavelength (radio, X-ray, gamma-ray, and neutrino) observations, will be a key experiment enabling us to discriminate between the two processes (cosmic-ray/electron origins), to locate and unravel the acceleration sites in our galaxy.

In the meanwhile, gamma rays above 100 TeV which is called Ultra-High-Energy (UHE) has not been detected until the Tibet AS $\gamma$  experiment succeeded in the first detection of gamma rays beyond 100 TeV from the Crab [4] at  $5.6 \sigma$ . Thus, the UHE gamma-ray astronomy started in 2019. The Crab UHE gamma-ray energy spectrum measured by the Tibet AS $\gamma$  experiment was confirmed by the HAWC [5], MAGIC [6], LHAASO [7] experiments later. Subsequently, a dozen of UHE gamma ray sources have been detected by the Tibet AS $\gamma$ , HAWC, LHAASO experiments, as of 2021. In this proceedings paper, the UHE gamma-ray sources, which have been detected by the Tibet AS $\gamma$  experiment so far after ICRC2019, are presented.

## 2. The Tibet AS $\gamma$ Experiment

The Tibet air shower experiment is an international joint experiment between China and Japan, which has been successfully operated at Yangbajing (90°31' E, 30°06' N; 4300 m above sea level) in Tibet, China since 1990 [8]. It has continuously made a wide field-of-view (approximately 2 steradian) observation of cosmic rays and gamma rays in the northern sky. After several upgrades, the current array (AS) [4] consists of 597 plastic scintillation detectors with an area of 0.5 m<sup>2</sup>, covering an area of 65,700 m<sup>2</sup>. The Tibet muon detector (MD) array (3,400 m<sup>2</sup> in total area) consists of 64 water-Cherenkov-type detectors located at 2.4 m underground of the AS array. Each detector is a waterproof concrete cell filled up with water of 1.5 m in depth, 7.35 m  $\times$  7.35 m in area, equipped with a 20-inch-diameter downward-facing photomultiplier tube (PMT) on the ceiling. A photon induced air shower has much less muons compared with a cosmic-ray induced

one. The Tibet MD array enables us to significantly discriminate a cosmic-ray background event from a photon signal by means of counting the number of muons in an air shower.

To generate air shower events in the atmosphere, employed are the CORSIKA code v7.4000 [9] with EPOS-LHC [[10]] for the high-energy hadronic interaction model and FLUKA code v2011.2b [11, 12] for the low-energy hadronic interaction model. The MC simulation [13] for the MD array considering the overburden has been developed based on the GEANT4 code [14]. The number of photoelectrons detected in the 20-inch PMT is converted to  $N_\mu$  referring to the single muon peak in each cell.

We reconstruct the arrival direction of an air shower by the relative timing information recorded at each scintillation detector. In the first place, we estimate the air shower core location weighted by  $\rho$ , where  $\rho$  is the number of particle density at each scintillation detector in an air shower. The relative timing  $t$ 's in the air shower front are fitted by a conical shape, and its cone angle is optimized by the MC simulation depending on the air shower size. The angular resolutions (50% containment) are estimated to be approximately  $0.5^\circ$  and  $0.2^\circ$  for 10 TeV and 100 TeV photon, respectively. The secondary particles in an air shower deposit energy, which is proportional to  $\rho$ , in a scintillator. The  $\rho$  at each detector is defined as the PMT output charge divided by the single particle peak which is monitored every 20 minutes to correct temperature dependence of each detector gain. The energy of each air shower is reconstructed using the lateral distribution of  $\rho$ , above 10 TeV. As an energy estimator, we use  $S50$  [15], which is defined as  $\rho$  at a distance of 50 m from the air shower axis in the best-fit Nishimura-Kamata-Greisen (NKG) function. The energy resolutions with  $S50$ , which depend on air shower core location and zenith angle, are roughly estimated to be 40% at 10 TeV and 20% at 100 TeV. On the other hand, the energy below 10 TeV was estimated directly from  $\Sigma\rho$  corresponding to the sum of of the particle density measured by each scintillation detector, as the number of hit detectors is too low to fit  $S50$ . The absolute energy scale uncertainty is estimated to be 12 % by the westward displacement of the Moon shadow position [16].

In this proceedings paper, we use data obtained by the Tibet air shower array combined with the muon detector array during 719 live days from 2014 February to 2017 May. The array configuration are the same as described in our previous paper [4].

### 3. Northern sky survey

In Fig.1, shown is the significance map in the northern sky survey using a point source searching mode (with small-size search windows dependent on energy) and “the Equi-zenith-angle Method” We find twelve gamma-ray point-like sources with more than  $5\text{-}\sigma$  significance, and all the gamma-ray sources are located along the galaxy disk.

We need to employ a different method from the point source search method for very extended  $\gamma$ -ray halos. We employ larger search windows and “the Equi-declination Method”. In Fig. 2, shown is the significance map around Geminga above 10 TeV, by employing  $3^\circ$  search window. One sees the excess emissions around the Geminga pulsar as well as around the south-east PSR B0656+14. For more details, see a reference [17].

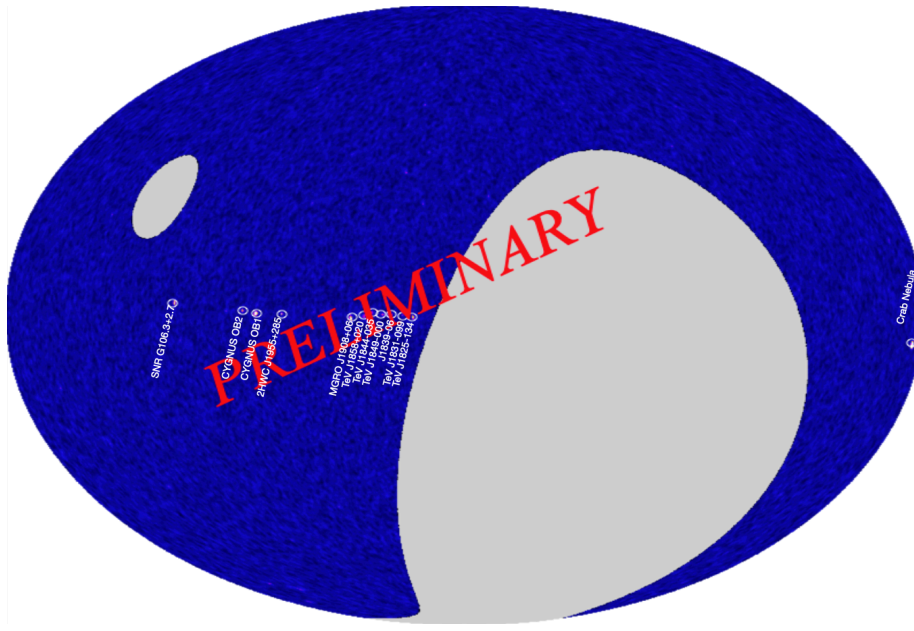


**Figure 1:** Figure from [17]. Significance map obtained by the northern sky gamma-ray survey with the Tibet ASy experiment in the galactic coordinates. White circles show the direction of event excess with significance more than  $5\sigma$  above 10 TeV. The gray region is outside of the field of view of the Tibet ASy experiment.

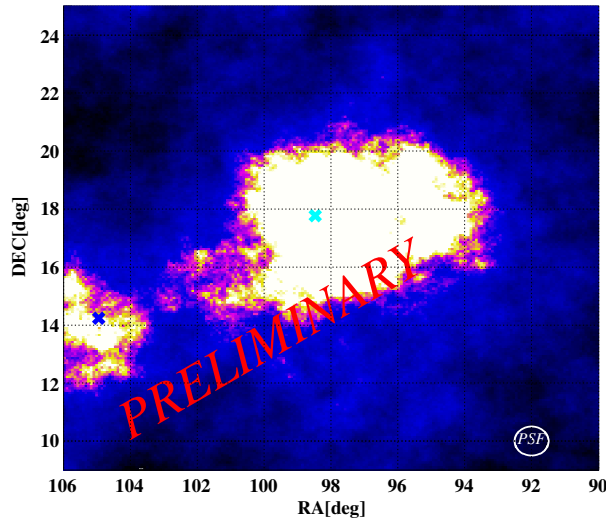


**Figure 2:** Figure from [17]. Significance map of the  $\gamma$ -ray emissions around Geminga. The cyan cross X shows the location of the Geminga pulsar. The blue cross X indicates the location of PSR B0656+14. The white circle in the bottom-right corner demonstrates the point spread function in the Tibet ASy experiment.

POS (ICRC2021) 015

## 4. Cygnus OB1 and OB2

The Cygnus region in the direction of the constellation Cygnus is an active star-forming region. There are many energetic gamma-ray sources such as SNRs, Pulsar Nebulae, Wolf-Rayet stars, open cluster, and OB associations, etc in the Cygnus region. The Cygnus region serves as a natural laboratory for studying cosmic-ray acceleration and propagation, and has been observed in a variety of wavelengths. The Cygnus-OB1 and Cygnus-OB2 regions, which have numerous hot and massive stars, are particularly the TeV gamma-ray sources. The first TeV gamma-ray source from Cygnus OB2 was J2032 + 4130 [18, 19] was discovered by the HEGRA experiment, and the Whipple [20], MAGIC [21], and VERITAS [22, 23] experiments confirmed the report. According to the report, the gamma-ray intensity is approximately 3% of the Crab gamma-ray flux with the source extension of roughly  $0.1^\circ$  to  $0.2^\circ$ . On the other hand, surface air shower array experiments report higher gamma-ray intensities than the IACTs' results in the multi-TeV energy region [24–28]. The flux discrepancy measured by IACT and the air shower array may be due to the morphological complexity of this region caused by the presence of gamma-ray sources such as Cygnus cocoon etc. The Fermi satellite-mounted LAT reported the existence of a region with strong gamma-ray intensity called "Cygnus cocoon" nearby Cygnus OB2. This is a star-forming region, and cosmic rays generated by star-forming activity are thought to be confined and accelerated in the interstellar space [29]. Cygnus Cocoon has a shape that connects Cygnus OB2 and NGC 6910, which is an open cluster and has a size of about 50 pc. It overlaps with the region of Cygnus OB2, which complicates morphology. The gamma-ray sources in this region are considered to be PWNs of PSR J2032+4127 and PSR J2021+4026 or SNR in Cygnus Cocoon, but the details are under debate.

In the Cygnus OB1 direction, the Milagro experiment discovered the MGRO J2019+37, which emits gamma rays exceeding 10 TeV [30], and was confirmed in the HAWC [31, 32] experiment. Also, VERITAS observed the same region above 0.6 TeV and separated the gamma-ray emissions into two sources: VER J2019+368 and VER J2016+371 [33]. At  $0.36^\circ$  east of the center of gravity of VER J2019 +368, there is a radio pulsar PSR J2021+3651 [34]. PSR J2021+3651 is one of the few pulsars with gamma-ray pulsations observed by Fermi-LAT [35], and also appears to form the pulsar wind nebula referred to as PWN G75.2+0.1 [36]. The radio and X-ray morphology of this nebula feature a bright bow-shaped tail extending westwards from the pulsar, indicating that the pulsar is moving eastwards with its birthplace as far west as the apparent end of the tail at  $0.2^\circ$  west of the current pulsar position [33, 37]. PSR J2021+3651/PWN G75.2+0.1 is considered to be the most promising object for VER J2019+368.

### 4.1 Cygnus OB2

Figure 3 (left figure) shows a detection significance map around the gamma-ray source detected by this work with photon energies above 10 TeV in the direction of Cygnus OB2. The sky is gridded in  $0.1^\circ \times 0.1^\circ$  pixels and the significance value of each pixel calculated according to [39] is smoothed by a circular search window of radius,  $R_w$ , centered at the pixel. Assuming a symmetrical 2D Gaussian distribution for the gamma-ray excess, we fit the events within the  $4^\circ \times 4^\circ$  region around the source using the unbinned maximum likelihood method. The centroid of gamma-ray emissions detected at the pre-trial (post-trial) detection significance of  $5.3\sigma$  ( $4.7\sigma$ ) above 10 TeV is estimated at (R.A., Dec.) =  $(308.04^\circ \pm 0.08^\circ, 41.46^\circ \pm 0.06^\circ)$ . We name this source TASG

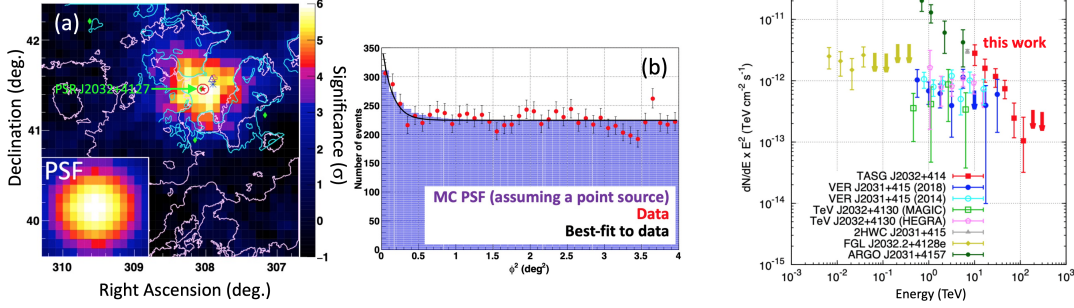
J2032+414. The location of TAsG J2032+414 is in good agreement with that of the pulsar PSR J2032+4127 and consistent with that of HAWC J2031+415 [40] at the  $1.7\sigma$  level, while it appears to deviate from that of TeV J2032+4130 reported in [41] at the  $2.8\sigma$  level.

Figure 3 (middle figure) shows the distribution of the number of events observed with photon energies above 10 TeV as a function of the square of the opening angle  $\phi$  between the estimated arrival direction and the centroid of TAsG J2032+414. To estimate a possible source extension, we perform the  $\chi^2$  fitting of the data with the function  $A \exp[-\phi^2/2(\sigma_{\text{PSF}}^2 + \sigma_{\text{EXT}}^2)] + N_{\text{BG}}$  where  $A$  and  $\sigma_{\text{EXT}}$  are two fitting parameters and  $\sigma_{\text{PSF}} = 0.36^\circ$  and  $N_{\text{BG}} = 224.5$  are the point spread function (PSF) of our instrument above 10 TeV and the number of background events estimated from the background cosmic-ray data, we get  $\sigma_{\text{EXT}} = 0.00^\circ \pm 0.14^\circ$ , which is consistent with that obtained from the maximum likelihood fitting described above. The  $\chi^2/\text{ndf}$  of the fitting is 33.8/38. With a large error of  $0.14^\circ$ , the  $\sigma_{\text{EXT}}$  value above 10 TeV does not indicate whether TAsG J2032+414 is extended or not even though it is consistent with the previous measurements at multi-TeV energies by IACTs, ARGO and HAWC within the  $2\sigma$  level [19, 21, 23, 26, 40, 41].

Figure 3(right figure) shows the differential energy spectrum of TAsG J2032+414. Although there is a discrepancy in flux at multi-TeV energies, our flux data points above 10 TeV are consistent with previous measurements of IACTs when the spill-over of gamma-ray signals outside their integration radius is taken into account. Our spectrum from 10 TeV to 120 TeV can be expressed by a simple power-law as  $dF/dE = N_0(E/40\text{TeV})^{-\Gamma}$  where  $N_0 = (4.13 \pm 0.83) \times 10^{-16} \text{TeV}^{-1} \text{cm}^{-2} \text{s}^{-1}$  is the differential gamma-ray flux at 40 TeV and  $\Gamma = 3.12 \pm 0.21$  is the spectral index ( $\chi^2/\text{ndf} = 1.6/4$ ). Unfortunately, the time span of our data does not cover the 2017 autumn periastron period of the binary system PSR J2032+4127/MT91 213 when a significant flare was detected in the TeV gamma-ray flux [41]. We find no significant flux variability in the time span of our data.

## 4.2 Cygnus OB1

Figure 4 (left figure) shows a significance map above 10 TeV in the direction of Cygnus OB1 obtained by this work. The centroid of gamma-ray emissions is estimated at (R.A., Dec.)  $= (304.99^\circ \pm 0.11^\circ, 36.84^\circ \pm 0.08^\circ)$  with the pre-trial (post-trial) detection significance of  $6.7\sigma$  ( $6.2\sigma$ ). We name this source TAsG J2019+368. The centroid of TAsG J2019+368 is consistent with that reported by HAWC [32] within the  $1\sigma$  level, and by VERITAS [23] within the  $2\sigma$  level. The pulsar PSR J2021+3651, located  $0.23^\circ$  east of the TAsG J2019+368 centroid, has a nebula extending westwards from the pulsar, PWN G75.2+0.1, which is coincident with the location of TAsG J2019+368. Figure 4 (middle figure) shows the angular distribution of the events observed above 10 TeV. The experimental data can be fitted with a Gaussian function with a source extension of  $\sigma_{\text{EXT}} = 0.28^\circ \pm 0.07^\circ$  above 10 TeV, consistent with the extension reported by VERITAS [23] (HAWC [31]) at the  $2.1\sigma$  ( $0.3\sigma$ ) level. The  $\chi^2/\text{ndf}$  of the fitting is 49.1/38. Figure 4 (right figure) shows the differential gamma-ray energy spectrum of TAsG J2019+368, which is in good agreement with the HAWC spectrum and connects with the VERITAS spectrum in 2014 reasonably. The spectrum in this work can be expressed either as  $dF/dE = N_0(E/40\text{TeV})^{-\Gamma}$  with  $N_0 = (10.6 \pm 1.3) \times 10^{-16} \text{TeV}^{-1} \text{cm}^{-2} \text{s}^{-1}$  and  $\Gamma = 2.70 \pm 0.13$  ( $\chi^2/\text{ndf} = 10.4/5$ ), or including an exponential cutoff as  $dF/dE = N_0(E/40\text{TeV})^{-\Gamma} \exp(-E/E_{\text{cut}})$  with  $N_0 = (3.6 \pm 2.0) \times 10^{-15} \text{TeV}^{-1} \text{cm}^{-2} \text{s}^{-1}$ ,  $\Gamma = 1.6 \pm 0.5$  and  $E_{\text{cut}} = 44 \pm 21 \text{TeV}$  ( $\chi^2/\text{ndf} = 3.0/4$ ). For more details, see [46, 47].



**Figure 3:** Figure from [46]. The gamma-ray emission source detected above 10 TeV in the directions of Cygnus OB2. The left figure is a significance map around the source, smoothed by search windows. The point spread function (PSF) is shown in the inset figure. The red-filled star with a position error circle is the centroid of TASG J2032+414 obtained by this work, while the magenta open cross is the centroid of VER J2031+415, and the blue asterisk is that of HAWC J2031+415. The green-filled diamonds show Fermi-LAT sources. The blue open triangle indicates the centroid of MAGIC J2031+4134. The green-filled diamond coincident with our gamma-ray emission centroid is the pulsar PSR J2032+4127. The sky-blue contours indicate 1420 MHz radio emissions provided by the Canadian Galactic Plane Survey, and the pink contours indicate 24  $\mu\text{m}$  infrared emissions by the Cygnus-X Spitzer Legacy Survey [42, 43]. The middle figure shows the distribution of the number of events observed with photon energies above 10 TeV as a function of the square of the opening angle between the estimated arrival direction and the centroid of TASG J2032+414. The red-filled circles are the experimental data, with the best fit Gaussian function indicated by the solid line. The blue histogram is the distribution of events expected by the MC simulation assuming a point-like gamma-ray source. The right figure shows the differential gamma-ray energy spectra of TASG J2032+414 with 95 % C.L. upper limits measured by this work (red filled squares/arrows). The blue-filled circles/arrows (sky-blue open circles) show the gamma-ray spectrum reported by VERITAS in 2018 (2014) [22, 23], the gray filled triangle by HAWC [28], and the dark-green filled circles by ARGO [26]. Additionally, the gold-filled diamonds are reported by Fermi-LAT [23], the green open squares by MAGIC [21], and the pink pentagons/arrow by HEGRA [19].

## 5. G106.3+2.7

G106.3+2.7, a supernova remnant, is an extended source discovered in the northern Galactic Plane survey by the Dominion Radio Astrophysical Observatory [48]. Located at the northeast edge of G106.3+2.7 is the so-called “Boomerang” pulsar wind nebula (PWN) G106.65+2.96, which is powered by an energetic ( $\dot{E} = 2.2 \times 10^{37} \text{ erg s}^{-1}$ ) pulsar PSR J2229+6114 of age 10.5 kyr [49, 50]. The radio and X-ray pulsations of PSR J2229+6114 were observed with a period of 51.6 ms [51]. The gamma-ray counterpart of PSR J2229+6114 was detected and named 0FGL J2229.0+6114 by the *Fermi* Large Area Telescope [52], and its  $\gamma$ -ray pulsations above 100 MeV were detected by *Fermi* [53] and AGILE [54]. Upper limits were given on the flux of PWN G106.65+2.96 between

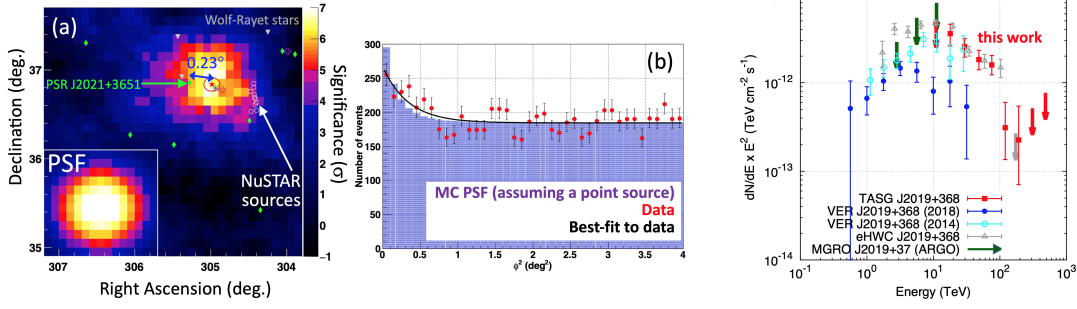


**Figure 4:** Figure from [46]. The gamma-ray emission sources detected above 10 TeV in the directions of Cygnus OB1. The left figure is a significance map around the source. The red-filled star with a position error circle is the centroid of TASG J2019+368 obtained by this work. The white open circles are NuSTAR X-ray sources [44], and the gray-filled inverted triangles are Wolf-Rayet stars [45]. The green-filled diamond located at  $0.23^\circ$  east of our emission centroid is the pulsar PSR J2021+3651. The magenta open cross located at (R.A., Dec.) = (303.99°, 37.21°) is another VERITAS source VER J2016+371 [23], which is not detected significantly in this work. The right figure shows the distribution of the number of events observed with photon energies above 10 TeV as a function of the square of the opening angle between the estimated arrival direction and the centroid of TASG J2019+368. The right figure shows the differential gamma-ray energy spectra of TASG J2019+368 with 95% C.L. upper limits measured by this work (red-filled squares/arrows). The blue-filled circles (sky-blue open circles) show the gamma-ray spectrum reported by VERITAS in 2018 (2014) [23, 33], the gray open triangles/arrow by HAWC [28, 31], and dark-green filled arrow by ARGO [26].

100 GeV and 1 TeV by the MAGIC experiment [55]. As discussed in [56], PSR J2229+6114 and SNR G106.3+2.7 could be the result of the same supernova explosion, and the radial velocity measurements of molecular material and atomic hydrogen suggested a distance of  $\sim 0.8$  kpc to the whole system.

By the Milagro experiment, detected was an elongated gamma-ray source MGRO J2228+61 coincident with PSR J2229+6114 at 35 TeV [57, 58]. Meanwhile, the VERITAS experiment detected gamma-ray emissions above 1 TeV from the supernova remnant (SNR) G106.3+2.7 with a flux of  $\sim 5\%$  Crab and named the source VER J2227+608 [59]. Recently the HAWC experiment observed G106.3+2.7 and reported a best-fit spectrum with an error band above 40 TeV [60]. The centroid of VER J2227+608,  $0.4^\circ$  away from PSR J2229+6114 in the southwest direction, is consistent with that of MGRO J2228+61 and the HAWC centroid within statistical plus systematic uncertainties. *Fermi* also observed this source at GeV energies and found that the source location is coincident with that of the molecular cloud [61].

Figure 5 (left figure) shows the detection significance map around G106.3+2.7 above 10 TeV, with smoothing by the search window size. The map is consistent with asymmetrical 2D Gaussian function, and the centroid of gamma-ray emissions (a red filled star with a red position error circle)

is at (R.A., Dec.) =  $(336.82^\circ \pm 0.16_{\text{stat}}, 60.85^\circ \pm 0.10_{\text{stat}})$ , coincident with a nearby molecular cloud location revealed by CO emissions (green contours) [64] overlying the black radio contours [62, 63] of the SNR and away from PSR J2229+6114 by  $0.44^\circ$  in the southwest direction. Our source location is also consistent with those of VERITAS [59] and HAWC [60]. Assuming the distance of 800 pc from the Earth to both PSR J2229+6114 and SNR G106.3+2.7, the distance from the pulsar to the source location obtained by this work is estimated at 6 pc. Our source location deviates from the pulsar location at a confidence level of  $3.1\sigma$ , based on the error of  $0.14^\circ$  including statistical errors as well as systematic ones. While the location of the HAWC centroid is consistent with both those of the Boomerang pulsar and the molecular cloud location, the centroids of VERITAS and Fermi are coincident with the location of molecular cloud as well as our source location.

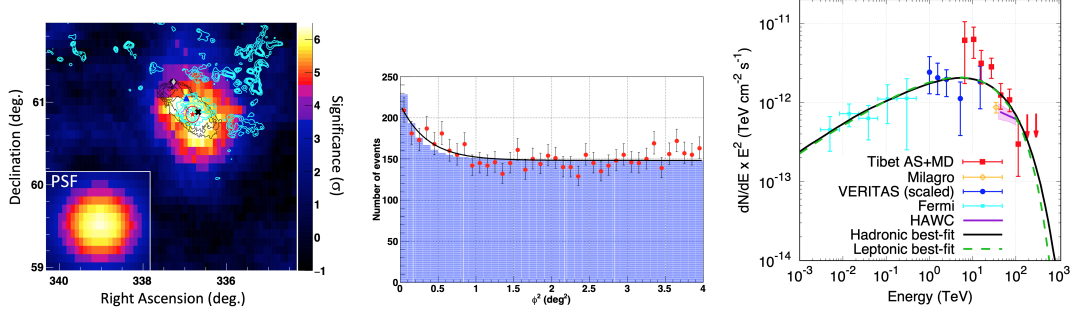


**Figure 5:** Figure from [69]. The left figure shows the significance map around SNR G106.3+2.7 observed by the Tibet ASy experiment above 10 TeV [70]. The red filled star with a  $1\sigma$  statistical position error circle is our source location, while the magenta open cross, the black X mark and the blue filled triangle are the centroids determined by VERITAS [59], Fermi [61] and HAWC [60]. The black contours represent 1420 MHz radio emissions from the Dominion Radio Astrophysical Observatory Synthesis Telescope [62, 63], and the cyan contours represent CO emissions from the Five College Radio Astronomy Observatory survey [64]. The gray filled diamond at the northeast corner of the black contours indicates the pulsar PSR J2229+6114. The inset figure shows our point spread function (PSF). The middle figure shows the projected angular distribution of events observed above 10 TeV [70]. The horizontal axis is  $\phi^2$  is the square of the opening angle between the estimated event arrival direction and our source location. The red filled circles are the experimental data with the best-fit black solid curve. The purple histogram is the expected event distribution by MC simulations assuming a point-like gamma-ray source. The right figure shows the differential gamma-ray energy spectrum of SNR G106.3+2.7 [70]. Red filled squares (Tibet AS+MD) represent data measured by this work with two 99 % C.L. upper limits (downward red arrows), VERITAS [59] (deep-blue filled circles), Fermi [61] (sky-blue crosses), Milagro [58] (an orange open diamond) and HAWC [60] (a purple solid line with a shaded light purple area indicating the  $1\sigma$  statistical error band). The VERITAS data points are raised by a factor of 1.62 from the original value [59]. The black solid (green dashed) line is the best-fit curve of the hadronic (leptonic) model for the combined data points of Tibet AS+MD, VERITAS and Fermi.

Figure 5 (middle figure) shows the distribution of the number of observed events above 10 TeV as a function of the opening angle between the measured arrival direction and our source location. Fitting the data with a Gaussian function +  $N_{\text{BG}}$ , assuming our point spread function is  $0.35^\circ$  above 10 TeV and  $N_{\text{BG}} = 148$  is the number of background events, we estimate the  $1\sigma$  extent of the source to be  $\sigma_{\text{EXT}} = 0.24^\circ \pm 0.10_{\text{stat}}^\circ$ , consistent with that estimated by VERITAS of  $0.27^\circ$  ( $0.18^\circ$ ) along the major (minor) axis.

Figure 5 (right figure) shows the differential gamma-ray energy spectrum (red filled squares

and two red downward arrows for two upper limits). The detection significance above 10 TeV is  $6.1\sigma$ . Our gamma-ray energy spectrum can be fitted by a single power law from 6 to 115 TeV as  $dN/dE = N_0(E/40 \text{ TeV})^{-\Gamma}$  with  $N_0 = (9.5 \pm 1.6_{\text{stat}}) \times 10^{16} [\text{cm}^{-2} \text{ s}^{-1} \text{ TeV}^{-1}]$  and  $\Gamma = 2.95 \pm 0.17_{\text{stat}}$  ( $\chi^2/\text{ndf} = 2.5/5$ ). The systematic error in  $N_0$  is estimated to be +40 %/-31 %, resulting from the 12 % uncertainty in the absolute energy scale determination. Our spectrum is consistent with the HAWC spectrum. The flux data points of VERITAS (blue filled circles) are raised by a factor of 1.62 to account for the spill-over of gamma-ray signals outside their window size. Our three flux data points below 20 TeV overlapping the energy range covered by the VERITAS flux points are statistically consistent with 1.62 times VERITAS original best-fit value at the  $1.5\sigma$  level.

As regards, the physical mechanism of the gamma-ray emission we fit the multi-wavelength gamma-ray energy spectrum using the *naima* [65] package. For the energy spectrum of the parent particles, we assume a power-law spectrum with an exponential cut off,  $E^{-\alpha} \exp(-E/E_{\text{cut}})$ . In the hadronic model, we get  $E_{\text{cut}} \sim 0.5 \text{ PeV}$  and  $\alpha \sim 1.8$ . The value  $\alpha$  falls between that predicted in the standard diffusive shock acceleration ( $\alpha = 2$ ) and the asymptotic limit [66, 67] of the very efficient proton acceleration ( $\alpha = 1.5$ ). The total energy of protons with energies  $> 1 \text{ GeV}$  ( $> 0.5 \text{ PeV}$ ) is estimated to be  $\sim 5.0 \times 10^{47} \text{ erg}$  ( $3.0 \times 10^{46} \text{ erg}$ ) for a target gas density of  $10 \text{ cm}^{-3}$ . One might argue that, considering the estimated SNR age of 10 kyr, PeV protons escape the SNR much earlier than the present time in the standard theory of cosmic-ray acceleration. Given that  $E_{\text{cut}} \sim 0.5 \text{ PeV}$  and that the maximum energy of protons remaining inside an SNR is proportional to  $\tau^{-0.5}$  [68] where  $\tau$  is the SNR age, protons should be accelerated up to  $\sim 1.6 \text{ PeV}$  at  $\tau = 1 \text{ kyr}$  in the case of G106.3+2.7. This suggests that the acceleration of protons at G106.3+2.7 should be efficient enough to push their maximum energy up to  $\sim 1.6 \text{ PeV}$  during the SNR free expansion phase. In addition, G106.3+2.7 has a dense molecular cloud nearby indispensable for accelerated protons to produce TeV gamma rays via  $\pi^0$  production. With  $\alpha \sim 1.8$ , the proton energy spectrum does not appear softened, implying that protons may not be able to escape the SNR easily due to the suppression of the diffusion coefficient. Future observations of G106.3+2.7 could provide useful information for these theoretical studies on its mechanisms of particle acceleration and confinement.

In the leptonic model, we get  $E_{\text{cut}} \sim 190 \text{ TeV}$ ,  $\alpha \sim 2.3$  and the SNR magnetic field strength of  $\sim 9 \mu\text{G}$ . The total energy of relativistic electrons with energies  $> 10 \text{ MeV}$  is estimated to be  $\sim 1.4 \times 10^{47} \text{ erg}$ . Considering the synchrotron cooling, we estimate that electrons need to be accelerated freshly within 1 kyr if they originate from the SNR, and that electrons provided by the Boomerang PWN are not likely to produce the observed gamma-ray emission in view of the energy budget and the gamma-ray morphology.

Generally, the energy spectrum of hadronically-induced gamma rays rises steeply below  $\sim 200 \text{ MeV}$  and approximately follows the energy spectrum of parent particles above a few GeV, resulting in a characteristic “ $\pi^0$ -decay bump” in the gamma-ray spectrum. Hopefully, future multi-wavelength observations would establish the hadronic origin of gamma-ray emissions from SNR G106.3+2.7.

Anyway, this is the first detection of gamma rays in the 100 TeV region from an overlapping region between a supernova remnant and a molecular cloud separated from a pulsar. For more details, see [69].

## 6. Sub-PeV diffuse galactic gamma rays

In order to extract diffuse gamma-ray signals in the large amount of cosmic-ray background events, we employ a tighter muon cut than in the point-like source analysis. With the tighter muon cut, we have succeeded in reducing the cosmic-ray background events down to approximately  $10^{-6}$  above 398 TeV. As a result, 38 gamma-ray-like events survive after the cut above 398 TeV, and 23 gamma-ray-like events are observed along the galactic disk within  $|b| < 10^\circ$  against low (2.73) cosmic-ray background events [71] estimated by real cosmic-ray data. Figure 6 shows the distribution of gamma-ray-like events above 398 TeV in the galactic coordinates. The coordinates in equatorial coordinates of the 38 gamma-ray-like events with  $398 < E < 1000$  TeV are listed in the supplemental material of [71]. The high galactic-latitude events ( $|b| > 20^\circ$ ) are assumed to be the cosmic-ray background events in this analysis. The highest-energy event among the 23 events along the galactic plane has unprecedentedly as high as 957 TeV, nearly 1 PeV. Surprisingly, the observed gamma rays above 398 TeV do not point back to any known TeV gamma-ray objects, but are ubiquitously spread over the galactic disk [71]. These spatially spread gamma rays are thought to have been produced by the interaction of cosmic-ray protons with the interstellar gas in our galaxy.

On the other hand, high-energy electrons interact with low-energy photons filled in our galaxy, and also produce ultra-high-energy (UHE) gamma rays (sub-PeV). However, UHE gamma rays of electron origin should be generated very close to a source and confined nearby it, as the electrons lose their energy rapidly and cannot travel far from their origin. Furthermore, the measured fluxes in the UHE region [71] are in reasonable agreement with a recent model [73] based on the hadronic cosmic-ray interactions, where UHE diffuse galactic gamma rays of electron origin is estimated to be negligible compared to those of cosmic-ray origin.

These arguments provide the first compelling evidence that cosmic rays, not electrons, were/are accelerated to PeV energies in our galaxy. This gives conclusive evidence for existence of cosmic-ray PeVatrons in the past and/or present galaxy. The existence of PeVatrons in our galaxy has been the subject of controversy for decades and is verified by this work. This work is also the first experimental proof of theoretical models that cosmic rays accelerated up to the “Knee” energy region are trapped by the magnetic field in our galaxy, forming a pool of cosmic rays.

In addition, four events out of the 23 gamma-ray-like events located within  $|b| < 10^\circ$  above 398 TeV concentrate in the Cygnus Cocoon region (around  $l = 80^\circ$ ,  $b = +1^\circ$  in Fig. 6), which is a very promising candidate for a PeVatron [27, 40, 74]. This work provides further strong evidence that the Cygnus Cocoon is a cosmic-ray source Pevatron. For more details, see [75].

Following the publication [71], many interpretation/discussion papers have appeared. Some of them are listed [76, 77] for further study.

## 7. Future prospect

As the Tibet ASy experiment is located in the northern hemisphere and monitors only the northern sky, the southern sky is out of field of view. Therefore, the southern sky has not been explored at sub-PeV energies. The next natural step is GO SOUTH. The ALPACA [79] experiment, similar to the Tibet ASy experiment is under construction. The construction of the proto-type experiment, ALPAQUITA [79] which is roughly 25 % of ALPACA, will be completed in 2021 or

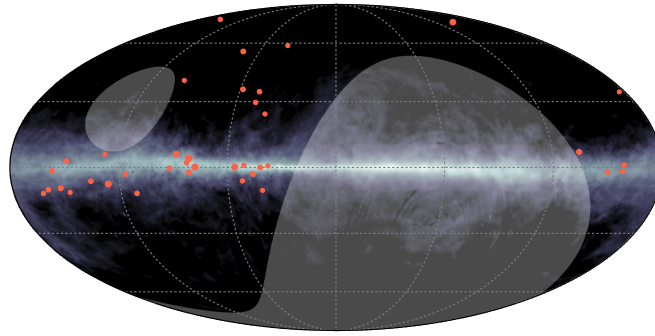


**Figure 6:** Figure from [75]. Distribution of gamma-ray-like events above 398 TeV (red points) in the galactic coordinates. The circle size is proportional to the gamma-ray energy. The background contour shows the atomic hydrogen distribution [72]. The gray shaded area indicates outside of the field of view of the Tibet ASy experiment.

2022, while the construction of ALPACA will be completed in 2022. ALPACA is expected to detect approximately a few tens of sources in the sub-PeV region during one-year operation. ALPACA will discriminate between the space-dependent and space-independent flux models of cosmic rays in our galaxy, as there is sizeable difference around the galactic center between the two models. In the future, CTA(south) [78], Mega ALPACA [79], SWGO [80] and other gamma-ray observatories are also planned in the southern hemisphere.

The UHE neutrino observations are also interesting. As the counter part of cosmic gamma rays, the cosmic neutrinos are emitted with a similar energy spectrum to that of gamma rays of cosmic ray origin. In the future, they will have sensitivity similar to the Tibet ASy experiment to the galactic sub-PeV sources, including sub-PeV diffuse galactic gamma rays and can provide alternative confirmation that the present sub-PeV sources detected by the Tibet ASy experiment are of cosmic-ray origin.

## Acknowledgements

The collaborative experiment of the Tibet Air Shower Arrays has been conducted under the auspices of the Ministry of Science and Technology of China and the Ministry of Foreign Affairs of Japan. This work was supported in part by a Grant-in-Aid for Scientific Research on Priority Areas from the Ministry of Education, Culture, Sports, Science and Technology, and by Grants-in-Aid for Science Research from the Japan Society for the Promotion of Science in Japan. This work is supported by the National Key R&D Program of China (No. 2016YFE0125500), the Grants from the National Natural Science Foundation of China (Nos. 11533007, 11673041, 11873065, 11773019, 11773014, 11633007, 11803011, and 11851305), and the Key Laboratory of Particle Astrophysics, Institute of High Energy Physics, CAS. This work is also supported by the joint research program of the Institute for Cosmic Ray Research (ICRR), the University of Tokyo.

## References

- [1] V. F. Hess, *Physikalische Zeitschrift* **14**, 1135 (1913).

- [2] G. V. Kulikov and G. B. Khristiansen, *J. Exp. Theor. Phys.* **35**, 635 (1958).
- [3] M. Ackermann et al, *Science* **339**, 807 (2013).
- [4] M. Amenomori et al., *Phys. Rev. Lett.* **123**, 051101 (2019).
- [5] A. U. Abeysekara et al., *ApJ* **881**, 134 (2019).
- [6] V. A. Acciari et al., *Astron. Astrophys.* **635**, A158 (2020).
- [7] Z. Cao et al., *Science* **373**, 425 (2021).
- [8] M. Amenomori et al., *Phys. Rev. Lett.*, **69**, 2468 (1992).
- [9] Heck, D., Knapp, J., Capdevielle, J. N., Schatz, G. & Thouw, T. CORSIKA: A Monte Carlo code to simulate extensive air showers. Report FZKA6019, Forschungszentrum Karlsruhe, (1998).
- [10] Pierog, T., Karpenko, Iu., Katzy, J. M., Yatsenko, E. & Werner, K. EPOS LHC: Test of collective hadronization with data measured at the CERN Large Hadron Collider, *Phys. Rev. C.* **92**, 034906-1-034906-15 (2015).
- [11] Böhflen, T. T. et al. The FLUKA code: Developments and challenges for high energy and medical applications. *Nuclear Data Sheets.* **120**, 211-214 (2014).
- [12] Ferrari, A., Sala, P. R., Fassò, A. & Ranft, J. FLUKA: A multi-particle transport code. CERN-2005-10, INFN/TC\_05/11, SLAC-R-773 (2005).
- [13] T. K. Sako et al., *Astropart. Phys.* **32**, 177 (2009).
- [14] Agostinelli, S. et al. Geant4 – a simulation toolkit. *Nucl. Instrum. Meth. A.* **506**, 250-303 (2003).
- [15] K. Kawata et al., *Experimental Astronomy*, **44**, 1 (2017)
- [16] M. Amenomori et al., *ApJ*, **692**, 61, (2009).
- [17] M. Amenomori et al., Proceedings of ICRC2021, Online/Berlin, Germany, July 12 - 23, 2021, Indico-ID1421, <https://pos.sissa.it/395/880> .
- [18] F. Aharonian et al., *Astron. Astrophys.* **393**, L37 (2002).
- [19] F. Aharonian et al., *Astron. Astrophys.* **431**, 197 (2005).
- [20] A. Konopelko et al., *Astrophys. J.* **658**, 1062 (2007).
- [21] J. Albert et al., *Astrophys. J. Lett.* **675**, L25 (2008).
- [22] E. Aliu et al., *Astrophys. J.* **783**, 16 (2014).
- [23] A. U. Abeysekara et al., *Astrophys. J.* **861**, 134 (2018).

- [24] A. A. Abdo et al., *Astrophys. J. Lett.* **664**, L91 (2007).
- [25] A. A. Abdo et al., *Astrophys. J.* **753**, 159 (2012).
- [26] B. Bartoli et al., *Astrophys. J. Lett.* **745**, L22 (2012).
- [27] B. Bartoli et al., *Astrophys. J.* **790**, 152 (2014).
- [28] A. U. Abeysekara et al., *Astrophys. J.* **843**, 40 (2017).
- [29] M. Ackermann et al., *Science* **334**, 1103 (2011).
- [30] A. A. Abdo et al., *Astrophys. J. Lett.* **658**, L33 (2007).
- [31] A. U. Abeysekara et al., *Phys. Rev. Lett.* **124**, 021102 (2020).
- [32] A. Albert et al., *Astrophys. J.* **905**, 76 (2020).
- [33] E. Aliu et al., *Astrophys. J.* **788**, 78 (2014).
- [34] M. S. E. Roberts, J. W. T. Hessels, S. M. Ransom, V. M. Kaspi, P. C. C. Freire, F. Crawford, and D. R. Lorimer, *Astrophys. J. Lett.* **577**, L19 (2002).
- [35] A. A. Abdo et al., *Astrophys. J.* **700**, 1059 (2009).
- [36] J. W. T. Hessels, M. S. E. Roberts, S. M. Ransom, V. M. Kaspi, R. W. Romani, C.-Y. Ng, P. C. C. Freire, and B. M. Gaensler, *Astrophys. J.* **612**, 389 (2004).
- [37] T. Mizuno, N. Tanaka, H. Takahashi, J. Katsuta, K. Hayashi, and R. Yamazaki, *Astrophys. J.* **841**, 104 (2017).
- [38] M. Amenomori et al., *Astrophys. J.* **633**, 1005 (2005).
- [39] T.-P. Li and Y.-Q. Ma, *Astrophys. J.* **272**, 317 (1983).
- [40] A. U. Abeysekara et al., *Nat. Astron. Lett.* **5**, 465 (2021).
- [41] A. U. Abeysekara et al., *Astrophys. J. Lett.* **867**, L19 (2018).
- [42] I. M. Beerer et al., *Astrophys. J.* **720**, 679 (2010).
- [43] K. E. Kraemer et al., *Astron. J.* **139**, 2319 (2010).
- [44] E. V. Gotthelf et al., *Astrophys. J.* **826**, 25 (2016).
- [45] K. A. van der Hucht, *New Astron. Rev.* **45**, 135 (2001).
- [46] M. Amenomori et al., Proceedings of ICRC2021, Online/Berlin, Germany, July 12 - 23, 2021, Indico-ID334, <https://pos.sissa.it/395/799>.
- [47] M. Amenomori et al., *Phys. Rev. Lett.* **127**, 031102 (2021).
- [48] G. Joncas & L. A. Higgs, *Astron. Astrophys. Suppl. Ser.* **82**, 113 (1990).

- [49] R. C. Hartman *et al.*, *Astrophys. J. Suppl. Ser.* **123**, 79 (1999).
- [50] Manchester, R. N., Hobbs, G. B., Teoh, A., & Hobbs, M., *Astron. J.* **129**, 1993 (2005).
- [51] J. P. Halpern *et al.*, *Astrophys. J.* **552**, L125 (2001).
- [52] A. A. Abdo *et al.*, *Astrophys. J. Suppl. Ser.* **183**, 46 (2009).
- [53] A. A. Abdo *et al.*, *Astrophys. J.* **706**, 1331 (2009).
- [54] Pellizzoni, A., *et al.*, *Astrophys. J.* **695**, L115 (2009).
- [55] H. Anderhub *et al.*, *Astrophys. J.* **710**, 828 (2010).
- [56] R. Kothes, B. Uyaniker & S. Pineault, *Astrophys. J.* **560**, 236 (2001).
- [57] A. A. Abdo *et al.*, *Astrophys. J.* **664**, L91 (2007).
- [58] A. A. Abdo *et al.*, *Astrophys. J.* **700**, L127 (2009).
- [59] V. A. Acciari *et al.*, *Astrophys. J.* **703**, L6 (2009).
- [60] A. Albert *et al.*, *Astrophys. J.* **896**, L29 (2020).
- [61] Y. Xin, H. Zeng, S. Liu, Y. Fan & D. Wei, *Astrophys. J.* **885**, 162 (2019).
- [62] A. R. Taylor *et al.*, *Astron. J.* **125**, 3145 (2003).
- [63] T. L. Landecker *et al.*, *Astron. Astrophys. Suppl. Ser.* **145**, 509 (2000).
- [64] M. H. Heyer *et al.*, *Astrophys. J. Suppl. Ser.* **115**, 241 (1998).
- [65] V. Zabalza, <https://arxiv.org/abs/1509.03319> (2015).
- [66] M. A. Malkov, *Astrophys. J.* **511**, L53 (1999).
- [67] E. G. Berezhko & D. C. Ellison, *Astrophys. J.* **526**, 385 (1999).
- [68] D. Caprioli, P. Blasi & E. Amato, *Mon. Not. R. Astron. Soc.* **396**, 2065 (2009).
- [69] M. Amenomori *et al.*, Proceedings of ICRC2021, Online/Berlin, Germany, July 12 - 23, 2021, Indico-ID1430, <https://pos.sissa.it/395/882> .
- [70] M. Amenomori *et al.*, *Nat. Astron. Lett.* **5** 460 (2021).
- [71] M. Amenomori *et al.*, *Phys. Rev. Lett.* **126**, 141101 (2021).
- [72] J. M. Dickey and F. J. Lockman, *HI in the Galaxy, Annual Rev. Astron. Astrophys.* **28**, 215 (1990).
- [73] P. Lipari and S. Vernetto, *Diffuse Galactic Gamma-ray Flux at Very High Energy, Phys. Rev. D* **98**, 043003 (2018).

- [74] F. Aharonian, R. Yang and E. de Oña Wilhelmi, *Nature Astronomy* **3**, 561 (2019).
- [75] M. Amenomori et al., Proceedings of ICRC2021, Online/Berlin, Germany, July 12 - 23, 2021, Indico-ID301, <https://pos.sissa.it/395/795> .
- [76] K. Fang and K. Murase, 2021, ariXiv e-prints, arXiv:2104.09491v2.
- [77] B. Qiao et al., 2021, arXiv e-prints, arXiv:2104.03729v1.
- [78] Cherenkov Telescope Array Consortium, Acharya, B. S., Agudo, I., et al. 2019, Science with the Cherenkov Telescope Array, arXiv e-prints, arXiv:1709.07997v2.
- [79] F. Aceves de la Cruz et al., Proceedings of ICRC2021, Online/Berlin, Germany, July 12 - 23, 2021, Indico-ID777, <https://pos.sissa.it/395/733> .
- [80] A. Albert et al., 2019, arXiv e-prints, arXiv:1902.08429.

### Full Authors List: The Tibet ASy Collaboration

M. Amenomori<sup>1</sup>, S. Asano<sup>2</sup>, Y. W. Bao<sup>3</sup>, X. J. Bi<sup>4</sup>, D. Chen<sup>5</sup>, T. L. Chen<sup>6</sup>, W. Y. Chen<sup>4</sup>, Xu Chen<sup>4</sup>, Y. Chen<sup>3</sup>, Cirennima<sup>6</sup>, S. W. Cui<sup>7</sup>, Danzengluobu<sup>6</sup>, L. K. Ding<sup>4</sup>, J. H. Fang<sup>4,8</sup>, K. Fang<sup>4</sup>, C. F. Feng<sup>9</sup>, Zhaoyang Feng<sup>4</sup>, Z. Y. Feng<sup>10</sup>, Qi Gao<sup>6</sup>, A. Gomi<sup>11</sup>, Q. B. Gou<sup>4</sup>, Y. Q. Guo<sup>4</sup>, Y. Y. Guo<sup>4</sup>, H. H. He<sup>4</sup>, Z. T. He<sup>7</sup>, K. Hibino<sup>12</sup>, N. Hotta<sup>13</sup>, Haibing Hu<sup>6</sup>, H. B. Hu<sup>4</sup>, K. Y. Hu<sup>4,8</sup>, J. Huang<sup>4</sup>, H. Y. Jia<sup>10</sup>, L. Jiang<sup>4</sup>, P. Jiang<sup>5</sup>, H. B. Jin<sup>5</sup>, K. Kasahara<sup>14</sup>, Y. Katayose<sup>11</sup>, C. Kato<sup>2</sup>, S. Kato<sup>15</sup>, T. Kawashima<sup>15</sup>, K. Kawata<sup>15</sup>, M. Kozai<sup>16</sup>, D. Kurashige<sup>11</sup>, Labaciren<sup>6</sup>, G. M. Le<sup>17</sup>, A. F. Li<sup>18,9,4</sup>, H. J. Li<sup>6</sup>, W. J. Li<sup>4,10</sup>, Y. Li<sup>5</sup>, Y. H. Lin<sup>4,8</sup>, B. Liu<sup>19</sup>, C. Liu<sup>4</sup>, J. S. Liu<sup>4</sup>, L. Y. Liu<sup>5</sup>, M. Y. Liu<sup>6</sup>, W. Liu<sup>4</sup>, X. L. Liu<sup>5</sup>, Y.-Q. Lou<sup>20,21,22</sup>, H. Lu<sup>4</sup>, X. R. Meng<sup>6</sup>, Y. Meng<sup>4,8</sup>, K. Munakata<sup>2</sup>, K. Nagaya<sup>11</sup>, Y. Nakamura<sup>15</sup>, Y. Nakazawa<sup>23</sup>, H. Nanjo<sup>1</sup>, C. C. Ning<sup>6</sup>, M. Nishizawa<sup>24</sup>, M. Ohnishi<sup>15</sup>, S. Okukawa<sup>11</sup>, S. Ozawa<sup>25</sup>, L. Qian<sup>5</sup>, X. Qian<sup>5</sup>, X. L. Qian<sup>26</sup>, X. B. Qu<sup>27</sup>, T. Saito<sup>28</sup>, Y. Sakakibara<sup>11</sup>, M. Sakata<sup>29</sup>, T. Sako<sup>15</sup>, T. K. Sako<sup>15</sup>, J. Shao<sup>4,9</sup>, M. Shibata<sup>11</sup>, A. Shiomi<sup>23</sup>, H. Sugimoto<sup>30</sup>, W. Takano<sup>12</sup>, M. Takita<sup>15</sup>, Y. H. Tan<sup>4</sup>, N. Tateyama<sup>12</sup>, S. Torii<sup>31</sup>, H. Tsuchiya<sup>32</sup>, S. Udo<sup>12</sup>, H. Wang<sup>4</sup>, Y. P. Wang<sup>6</sup>, Wangdui<sup>6</sup>, H. R. Wu<sup>4</sup>, Q. Wu<sup>6</sup>, J. L. Xu<sup>5</sup>, L. Xue<sup>9</sup>, Z. Yang<sup>4</sup>, Y. Q. Yao<sup>5</sup>, J. Yin<sup>5</sup>, Y. Yokoe<sup>15</sup>, N. P. Yu<sup>5</sup>, A. F. Yuan<sup>6</sup>, L. M. Zhai<sup>5</sup>, C. P. Zhang<sup>5</sup>, H. M. Zhang<sup>4</sup>, J. L. Zhang<sup>4</sup>, X. Zhang<sup>3</sup>, X. Y. Zhang<sup>9</sup>, Y. Zhang<sup>4</sup>, Yi Zhang<sup>33</sup>, Ying Zhang<sup>4</sup>, S. P. Zhao<sup>4</sup>, Zhaxisangzhu<sup>6</sup> and X. X. Zhou<sup>10</sup>

<sup>1</sup>Department of Physics, Hirosaki University, Hirosaki 036-8561, Japan. <sup>2</sup>Department of Physics, Shinshu University, Matsumoto 390-8621, Japan. <sup>3</sup>School of Astronomy and Space Science, Nanjing University, Nanjing 210093, China. <sup>4</sup>Key Laboratory of Particle Astrophysics, Institute of High Energy Physics, Chinese Academy of Sciences, Beijing 100049, China. <sup>5</sup>National Astronomical Observatories, Chinese Academy of Sciences, Beijing 100012, China. <sup>6</sup>Department of Mathematics and Physics, Tibet University, Lhasa 850000, China. <sup>7</sup>Department of Physics, Hebei Normal University, Shijiazhuang 050016, China. <sup>8</sup>University of Chinese Academy of Sciences, Beijing 100049, China. <sup>9</sup>Institute of Frontier and Interdisciplinary Science and Key Laboratory of Particle Physics and Particle Irradiation (MOE), Shandong University, Qingdao 266237, China. <sup>10</sup>Institute of Modern Physics, SouthWest Jiaotong University, Chengdu 610031, China. <sup>11</sup>Faculty of Engineering, Yokohama National University, Yokohama 240-8501, Japan. <sup>12</sup>Faculty of Engineering, Kanagawa University, Yokohama 221-8686, Japan. <sup>13</sup>Faculty of Education, Utsunomiya University, Utsunomiya 321-8505, Japan. <sup>14</sup>Faculty of Systems Engineering, Shibaura Institute of Technology, Omiya 330-8570, Japan. <sup>15</sup>Institute for Cosmic Ray Research, University of Tokyo, Kashiwa 277-8582, Japan. <sup>16</sup>Institute of Space and Astronautical Science, Japan Aerospace Exploration Agency (ISAS/JAXA), Sagami-hara 252-5210, Japan. <sup>17</sup>National Center for Space Weather, China Meteorological Administration, Beijing 100081, China. <sup>18</sup>School of Information Science and Engineering, Shandong Agriculture University, Taian 271018, China. <sup>19</sup>Department of Astronomy, School of Physical Sciences, University of Science and Technology of China, Hefei 230026, China. <sup>20</sup>Department of Physics and Tsinghua Centre for Astrophysics (THCA), Tsinghua University, Beijing 100084, China. <sup>21</sup>Tsinghua University-National Astronomical Observatories of China (NAOC) Joint Research Center for Astrophysics, Tsinghua University, Beijing 100084, China. <sup>22</sup>Department of Astronomy, Tsinghua University, Beijing 100084, China. <sup>23</sup>College of Industrial Technology, Nihon University, Narashino 275-8576, Japan. <sup>24</sup>National Institute of Informatics, Tokyo 101-8430, Japan. <sup>25</sup>National Institute of Information and Communications Technology, Tokyo 184-8795, Japan. <sup>26</sup>Department of Mechanical and Electrical Engineering, Shandong Management University, Jinan 250357, China. <sup>27</sup>College of Science, China University of Petroleum, Qingdao 266555, China. <sup>28</sup>Tokyo Metropolitan College of Industrial Technology, Tokyo 116-8523, Japan. <sup>29</sup>Department of Physics, Konan University, Kobe 658-8501, Japan. <sup>30</sup>Shonan Institute of Technology, Fujisawa 251-8511, Japan. <sup>31</sup>Research Institute for Science and Engineering, Waseda University, Tokyo 162-0044, Japan. <sup>32</sup>Japan Atomic Energy Agency, Tokai-mura 319-1195, Japan. <sup>33</sup>Key Laboratory of Dark Matter and Space Astronomy, Purple Mountain Observatory, Chinese Academy of Sciences, Nanjing 210034, China.